ACS APPLIED MATERIALS & INTERFACES

www.acsami.org

Research Article

Nanoscale Topography of Anodic TiO_2 Nanostructures Is Crucial for Cell–Surface Interactions

Jung Park,[#] Alexander B. Tesler, Ekaterina Gongadze, Aleš Iglič, Patrik Schmuki, and Anca Mazare*[,#]

Cite This: *ACS Appl. Mater. Interfaces* 2024, 16, 4430–4438

Read Online

ACCESS | Metrics & More | Article Recommendations | Supporting Information

ABSTRACT: Anodic titanium dioxide (TiO_2) nanostructures, i.e., obtained by electrochemical anodization, have excellent control over the nanoscale morphology and have been extensively investigated in biomedical applications owing to their sub-100 nm nanoscale topography range and beneficial effects on biocompatibility and cell interactions. Herein, we obtain TiO_2 nanopores (NPs) and nanotubes (NTs) with similar morphologies, namely, 15 nm diameter and 500 nm length, and investigate their characteristics and impact on stem cell adhesion. We show that the transition of TiO_2 NPs to NTs occurs via a pore/wall splitting mechanism and the removal of the fluoride-rich layer. Furthermore, in contrast to the case of NPs, we observe increased cell adhesion and proliferation on nanotubes. The enhanced mesenchymal stem cell adhesion/proliferation seems to be related to a 3-fold increase in activated integrin clustering, as confirmed by immunogold labeling with β1 integrin antibody on the nanostructured layers. Moreover, computations of the electric field and surface charge density show increased values at the inner and outer sharp edges of the top surfaces of the NTs, which in turn can influence cell adhesion by increasing the bridging interactions mediated by proteins and molecules in the environment. Collectively, our results indicate that the nanoscale surface architecture of the lateral spacing topography can greatly influence stem cell adhesion on substrates for biomedical applications.

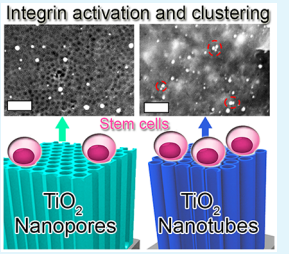

KEYWORDS: *TiO2 nanotubes, TiO2 nanopores, anodization, surface topography, stem cells, integrin*

1. INTRODUCTION

Nanometric scale surface topography and the roughness of biomimetic and implant materials are critical factors for cell attachment and survival.[1−3] Titanium (Ti) and its alloys have been extensively investigated as implant materials because of their unique combination of properties, including high biocompatibility, good tensile strength, improved corrosion resistance, and excellent nanostructuring.[4−6] Modifying the nanoscale surface, physical properties, and surface chemistry of Ti and Ti alloys largely affects the material biocompatibility and cell−substrate interactions.[3,7−14]

Typical surface modification techniques for Ti and its alloys include for example mechanical modification (such as grinding),[15] chemical etching,[16,17] sandblasting,[18] various deposition techniques (evaporation,[19] sputtering,[20] chemical vapor deposition,[21] atomic layer deposition[17,21,22]), and electrochemical anodization.[2] Electrochemical anodization is one of the most commonly used techniques for nanoscale surface modifications, due to its ease of use and nanoscale control, allowing the formation of nanostructures directly on Ti metal and its alloys.[2,23,24] To date, a variety of titanium dioxide (TiO_2) nanostructures can be fabricated as a function of the anodization parameters, including nanotubes (NTs[2,25] or single NTs dispersed by ultrasonication[26]), nanopores (NPs),[27,28] nanochannels,[29,30] dispersed nanocylinders,[26] and nanopillars.[31] Through extensive investigation for decades, anodic TiO_2 nanotubes can offer excellent control over NT diameter in the sub-100 nm range (for an overview, see refs 2, 3, 11, 23, and 32), and various nanotube morphologies such as nanotubes with a thin initiation layer, open-top nanotubes, single-wall or double-wall morphology, multilayers, and spaced nanotubes have been developed.[2,23] In addition, the nanostructured surfaces can be also modified for targeted biomedical applications, in terms of (i) additional bioactive layers, e.g., hydroxyapatite with a subsequent deposition step or via a one-step process based on microarc oxidation,[33,34] or hydrothermal based treatments,[35] (ii) coated with various inorganic or organic layers (TiO_2,[36] organic monolayers[37]), (iii) decorated with various nanoparticles,[38] (iv) functionalized with organic molecules, peptides, drugs, etc.,[39] (v) via various annealing treatments.[40,41] Such modifications can further increase the cell activity and increase osseointegration or antibacterial activity of the various TiO_2 nanostructured layers, as well as influencing the TiO_2 NT/cell interface.[42]

Regarding the impact of the NT's morphology on cell interactions, literature data show that this depends on the cell plating density (5×10^3 to 5×10^4 or even higher) on the surface of the sample (and on the sterilization procedure),[43−45] with lower cell plating densities (e.g., 5×10^3) indicating that

Received: October 27, 2023
Revised: December 13, 2023
Accepted: December 19, 2023
Published: January 17, 2024

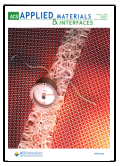

https://doi.org/10.1021/acsami.3c16033
ACS Appl. Mater. Interfaces 2024, 16, 4430−4438

diameters below 30 nm are optimal and for higher densities or changes in the tube morphology or properties (due to sterilization), it is larger tube diameters. Park et al.[1,46−49] reported that the optimum NT diameter for increased cell interactions (adhesion/proliferation) of cells such as mesenchymal stem cells (MSC), endothelial cells, etc., is 15 nm, confirmed also by Brammer et al.[50] reporting the highest degree of cell activity (osteoblasts) for 30 nm NTs, whereas Chamberlain et al.[8] show a reduced inflammatory response for 70 nm NTs and Li et al.[51] a cell activity decrease with increasing NT diameter. Recently, Shen et al.[43] confirmed that the diameter effect on cell adhesion and proliferation depends on cell plating and sterilization approach. In addition, Khaw et al.[52] reported that different cell lines also have an effect, with human MSC showing osteogenic differentiation on 20 nm NTs, while human osteoblasts showed osteoblastic maturation on 50 nm NTs.

In the case of the optimal 15 nm tube diameter for cell activity, this was attributed to the best fit of the lateral spacing distance of nanotubes to the predicted size of integrin receptors (∼10 nm) at the cell−nanotube interface, leading to optimal integrin activation, allowing favorable cell anchoring to the NTs surface. Moreover, one aspect not yet elucidated is related to the different morphologies of NPs or NTs and more so in the case of NTs, i.e., covered with a thin initiation porous layer (so similar at the top with NPs) or open-top NTs. It is still not completely elucidated whether cell proliferation on the NT surface can be regulated mainly by NT diameters or also can be greatly affected or further supported by other topographical cues including TiO_2 surface area/roughness independent of tube diameters. Therefore, we investigate the impact of differential top surface morphologies of the nanostructures with comparable NT diameters on cell adhesion and proliferation by analyzing integrin clustering and focal contact formation in the cytoskeletons of human mesenchymal stem cells (MSCs).

Herein, we report the anodic growth of NPs and NTs with a tube diameter of ∼15 nm. We identify the morphological and chemical characteristics of each topography and show evidence of a transition from NPs to NTs through the fluoride-rich layer. The optimized anodic TiO_2 nanostructures are evaluated in terms of their effect on mesenchymal stem cells and, more specifically, on integrin activation. Furthermore, numerical simulations evaluate the electric field and surface charge density of the nanostructures. The present data clearly show how the top surface morphology of the nanostructures influences integrin adhesion and the formation of focal contacts, thus critical in cell interaction.

2. EXPERIMENTAL SECTION

2.1. Nanostructure Formation. TiO_2 nanotubes are obtained by electrochemical anodization in a two-electrode electrochemical cell with Pt as the cathode and Ti foil as the anode. Ti foils are cleaned by ultrasonication in acetone and ethanol (5 min each), rinsed with distilled water, and dried under a nitrogen stream. A two-step anodization approach is used (as a surface pretreatment) to ensure high ordering of the nanostructures. Briefly, the Ti foil is anodized at 35 V for 2 h in ethylene glycol + 0.1 M NH_4F + 1 M H_2O. The obtained nanotubes are removed by ultrasonication, resulting in a prepatterned surface that is subsequently used in actual anodization. The optimal anodization parameters consist of using an ethylene glycol-based electrolyte (EG + 0.2 M HF + 4 M H_2O) at 10 V for 5 h (nanopores) and 13 h (nanotubes). EG and HF 40% were purchased from Sigma-Aldrich. All the electrolytes are prepared from reagent-grade chemicals and deionized water.

2.2. Characterization. (a) Field emission SEM (FESEM, S-4800, Hitachi) equipped with an energy-dispersive X-ray spectroscope (EDAX, Genesis) was used for the morphological characterization of the sample surfaces. The nanostructures' morphology is measured on 10 different 200k magnification images of the two nanostructured samples. Histograms are plotted in Origin 8.0, and the mean values are determined.

(b) The crystallographic properties of the materials are analyzed by X-ray diffraction (XRD) using an X'pert Philips MPD (equipped with a Panalytical X' celerator detector) with graphite-monochromized Cu Kα radiation (λ = 1.540 56 Å).

(c) The chemical compositions of the samples are analyzed by X-ray photoelectron spectroscopy (XPS, PHI 5600), and the spectra are shifted according to the Ti 2p signal at 459.0 eV in the MultiPak software. Depth profiling is carried out using an Ar^+ sputter source at a sputtering angle of 45° to the surface normal and a sputter rate of 5.1 nm/min. Sputter steps of 2 min are repeated, and the atomic composition is determined between consecutive sputtering intervals using the peak area in the MultiPak software. The sputtering rate is calibrated using commercial Si/SiO_2 wafers (Si(100) p-type with 100 nm of SiO_2, μChemicals, Germany).

(d) Time-of-flight secondary ion mass spectrometry (ToF-SIMS) negative depth profiles are measured on a ToF SIMS 5 instrument (ION-TOF, Münster, Germany) in a dual beam mode and pulsed 25 keV Bi^+ liquid−metal ion beam (<0.8 ns) for spectra generation and a 2 keV Cs^+ ion beam for sputter removal, with a 350 × 350 μm^2 sputter crater and measuring in the center 65.6 × 65.6 μm^2 area. The mass fragment signals are identified based on their exact masses and isotopic patterns. The spectra are calibrated, and Poisson correction is used.

(e) A contact angle measurement system (DSA100, KRÜSS, Germany) is used for the water contact angle measurements at room temperature. The droplet volume used for the measurements is 10 μL, and the macroscopic droplet profile is captured using a camera. The droplet profile is fitted by a Drop Shape Analysis computer program provided by the manufacturer. At least three independent measurements are averaged for all of the contact angle values specified in the text.

2.3. Cell Culture. Previously established clonal human mesenchymal stem cells (MSC)[1] labeling with green fluorescent protein (GFP)[53] were cultured and used for the present experiments. The GFP-labeled mesenchymal stem cells were cultured initially in the appropriate stem cells medium containing 60% DMEM-LG (Gibco BRL), 40% MCDB-201 (Sigma), and supplemented with 1× insulin-transferrin-selenium (Sigma), 1× linoleic-acid-bovine-serum-albumin (Sigma), 10 nM dexamethasone (Sigma), 100 μM ascorbic acid 2-phosphate (Sigma), 100 units of penicillin, 1000 units of streptomycin (Life Technologies), 10 ng/mL epidermal growth factor (EGF Sigma), 10 ng/mL platelet derived growth factor-BB (PDGF-BB, R&D Systems), and 1000 units/mL of leukemia inhibitory factor (LIF, Thermo Fisher Scientific), 2% fetal calf serum (FCS, Hyclone Laboratories). The mesenchymal stem cells were seeded directly onto the surface of the analyzed samples at cell densities of 5000 cm^{-2}. For cell adhesion experiments, 24 h after cell plating, nonadherent cells are washed with phosphate buffered saline (PBS), adherent cells are counted in six different areas (1280 × 1024 pixels), and each sample is visualized under a fluorescent microscope (25× magnification). Cell proliferation is quantified 3 days after cell plating by cell counting using the same approach with a Zen image analyzer (Zeiss). Cell count data are combined into one mean and standard deviation for each sample.

2.4. Immunogold Staining. For immunogold staining, 1 day after cell plating, the cells are fixed with 2% paraformaldehyde (PFA) for 10 min and washed with PBS, including 0.2 mM glycin. The cells are permeabilized with 0.2% Triton X-100 in PBS for 2 min and then washed with PBS. The samples are blocked with bovine serum albumin (BSA) and incubated with the primary antibody, mouse monoclonal antiintegrin β1 (Invitrogen), for 1 h. After washing with

https://doi.org/10.1021/acsami.3c16033
ACS Appl. Mater. Interfaces 2024, 16, 4430−4438

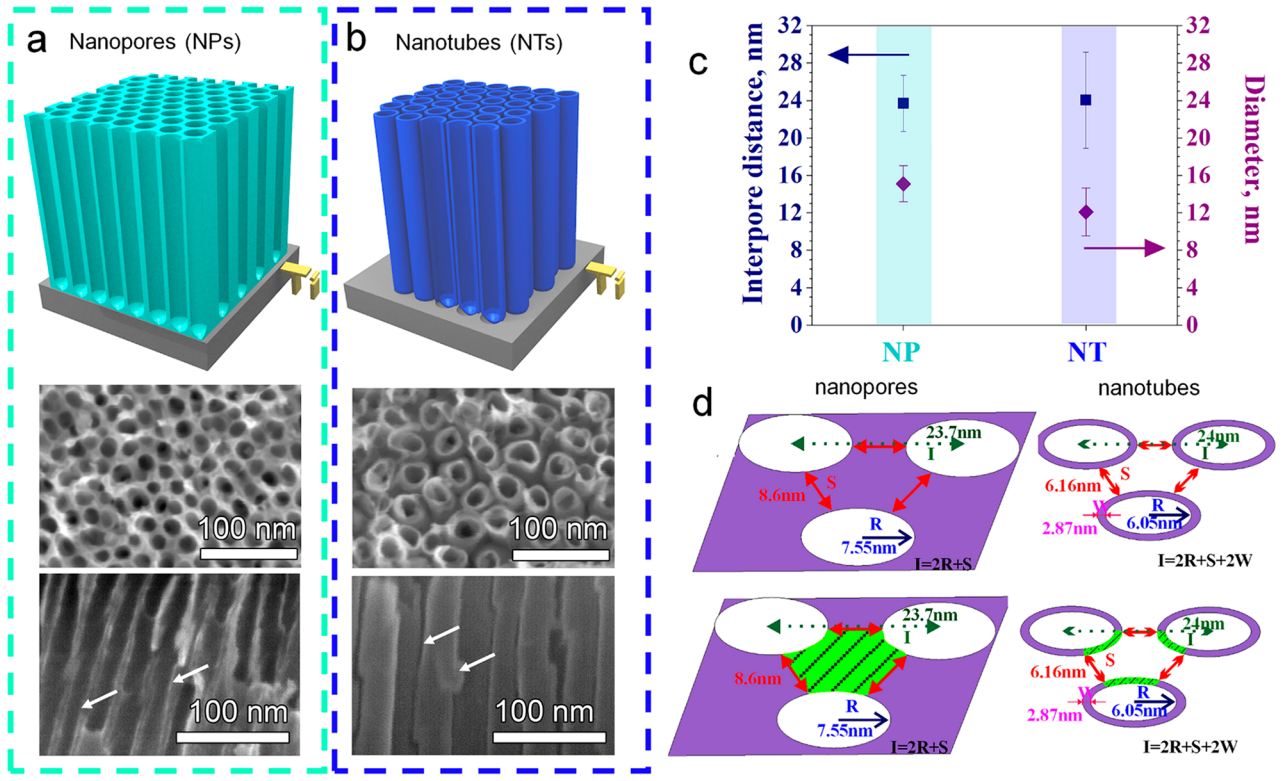

Figure 1. Schematic representation of the (a) NPs and (b) NTs, together with corresponding top-view and cross-sectional SEM images, with the lowest panels showing the side wall view of the nanostructures (scale bar 100 nm). (c) Mean interpore distance and diameter values for the NP and NT nanostructures. (d) Graphic representation of the nanostructure morphology (TiO_2 surface area in purple) and the top surface area available per unit area (highlighted in green).

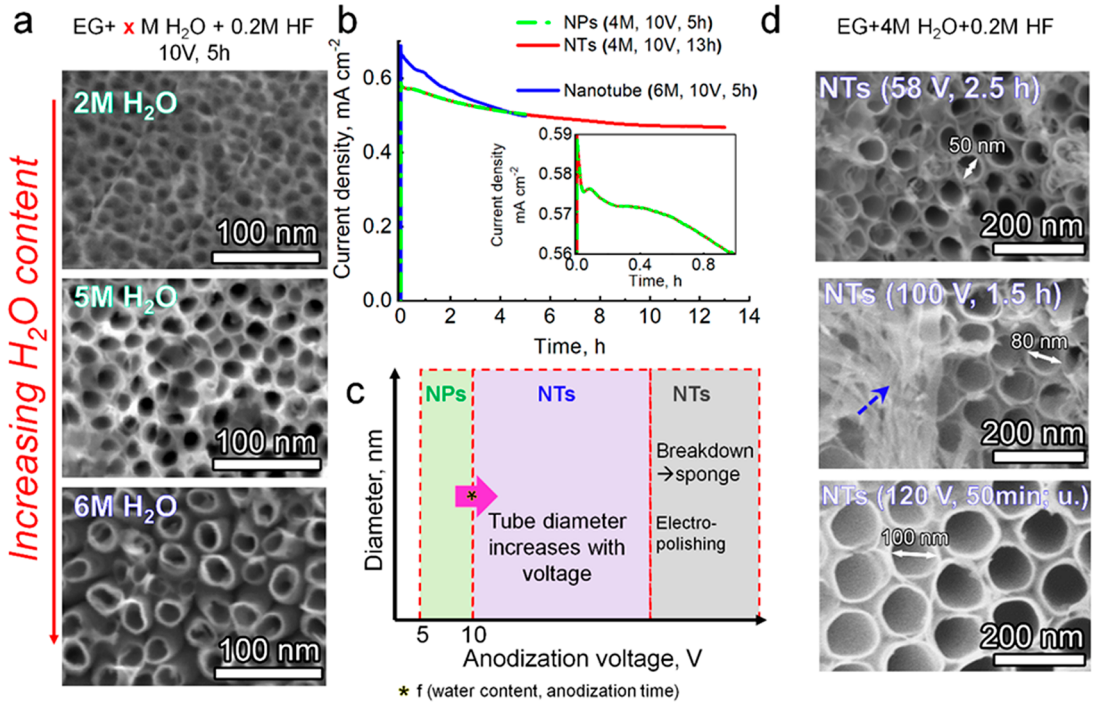

Figure 2. Optimized morphology control: (a) SEM images of nanostructures obtained in EG + *x* M H_2O + 0.2 M HF at 10 V for 5 h (*x* H_2O:2 M NPs, 5 M NPs, and 6 M NTs; scale bar 100 nm). (b) Current density profiles for selected samples: NPs (4 M, 10 V, 5 h), NTs (4 M, 10 V, 13 h), NTs − 1 (EG + 6 M H_2O + 0.2 M HF, 10 V, 5 h). (c) NP and NT growth regions. (d) NTs in EG + 4 M H_2O + 0.2 M HF: 50 nm diameter NTs (58 V, 2.5 h), 80 nm diameter NTs with nanograss; see arrow (100 V, 1.5 h), 100 nm diameter NTs with mild postultrasonication treatment (100 V, 1.5 h); scale bar 200 nm.

https://doi.org/10.1021/acsami.3c16033
ACS Appl. Mater. Interfaces 2024, 16, 4430−4438

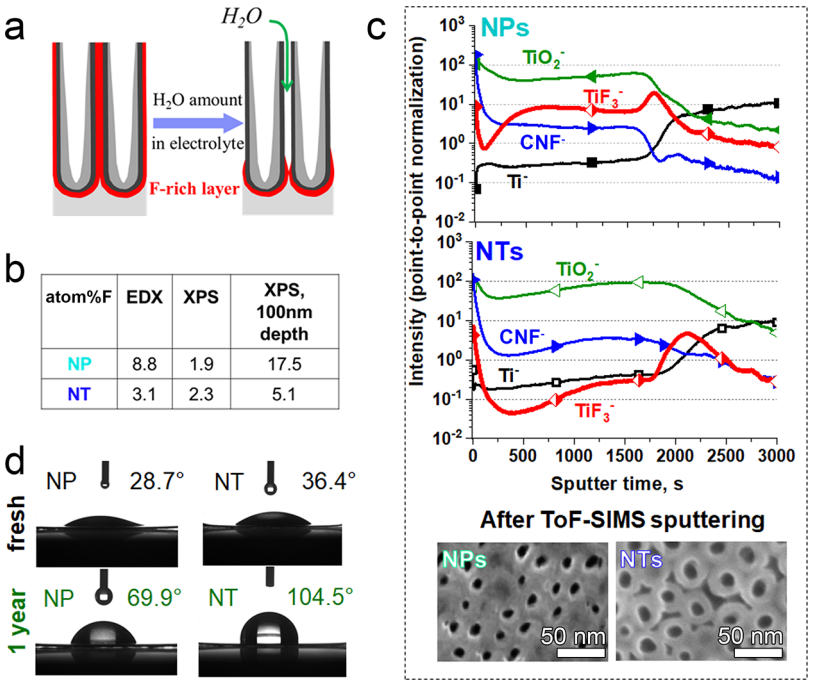

Figure 3. (a) Formation of NTs from an initial NP morphology (via selective dissolution of F-rich layers and preferential etching by the water in the electrolyte). (b) Atomic percentage (atom %) of F from EDX and XPS. (c) ToF-SIMS sputter depth profiles for selected mass fragments of Ti^-, TiO_2^-, CNF^-, and TiF_3^- and high-resolution SEM images after sputtering (scale bar 50 nm). (d) Contact angle of nanostructures (fresh and after 1 year).

PBS, the samples are incubated with 10 nm gold particle-conjugated antimouse IgG and M antibody diluted 1:30 in PBS for 1 h, followed by washing with PBS. For SEM observation, the cells are fixed with a 2.5% glutaraldehyde (GTA) solution (Merck) overnight at 4 °C. Samples are rinsed in PBS solution, dehydrated in a series of acetone solutions (60, 70, 80, 90, and 100%), and critical point dried with a Critical Point Dryer (CPD 030, Balzers).

2.5. Modeling. The electric field and surface charge density on the charged 3D surface in contact with the electrolyte solution are calculated using the modified Langevin−Poisson−Boltzmann model and numerically computed using COMSOL Multiphysics 6.0.[54,55] The condition of a constant electric potential on the surface is imposed in the numerical calculations

2.6. Statistical Analysis. Differences between data sets of individual values from NP and NT cell proliferation and immunogold staining were analyzed with unpaired *t* tests using the GraphPad Prism software 9 (GraphPad Software Inc., La Jolla, USA).

3. RESULTS AND DISCUSSION

A typical 3D schematic representation of the TiO_2 NP and NT structures obtained by electrochemical anodization is shown in Figure 1a,b. These layers are obtained by anodization in a fluoride-containing electrolyte with low water content (EG + 0.2 M HF + 4 M H_2O) at a low voltage of 10 V for 5 h for NPs and 13 h for NTs, and the double-anodization approach[3] leads to highly ordered layers (see Figure S1). The major difference between the two structures lies in the spacing or separation between the NTs, which is not observed in the NPs. This specific difference in the structure is easily seen in the top-view and cross-sectional SEM images throughout the entire 500 nm length; see Figure 1a,b arrows.

The mean diameter and interpore distance for NP and NT layers are in the range of 12−16 nm and 22−26 nm, respectively (Figure 1c). A graphical representation of the morphology and active top surface area of the NTs and NPs (Figure 1d) and computational calculations indicate that NPs have a higher top active surface area (0.60 cm^2 per 1.00 cm^2 sample) compared to NTs (0.10 cm^2).

Typical NTs obtained in most organic electrolytes have a smooth thin nanopore/nanoring array or initiation layer covering the NTs tops, as shown in Figure S2, and such NTs differ from NPs. Such layers are grown on metallic Ti substrates in ethylene glycol electrolytes using ammonium fluoride (either on as-is or polished Ti, or in a one-step or two-step anodization approach),[56−60] which are often reported as nanoporous structures.[61,62] Thus, SEM cross-sectional images of the nanostructured layers are beneficial to verifying the nature of the anodic layer.

Since the goal of the current work is to evaluate the influence of two different morphologies with similar-size diameters on cell interactions, it is imperative for both NP and NT nanostructures to have similar morphological characteristics, especially inner diameter. The crucial parameters for controlling the anodization parameters to obtain NPs or NTs are the water content in the electrolyte, applied voltage, and anodization time, and decisive is the solubility of the cell boundaries (fluoride-rich) in the anodization electrolytes.[27,63]

The nanopore-to-nanotube transition can be controlled by increasing water content as shown in the SEM images of Figure 2a, namely, in low-water content electrolytes, the transition from a porous to a tubular morphology is gradual, while higher water contents lead to faster dissolution of the fluoride-rich layer and thus to splitting of the porous layer into a tubular one. Optimized nanostructures are obtained in a 4 M water content electrolyte at 10 V for 5 h for NPs and 13 h for NTs (see the Experimental Section for more details). Under similar anodization conditions (10 V, 5 h), increasing the water content in the electrolyte from 2 to 6 M results in a transition from NPs to NTs (Figures 1a and 2a). A lower water content

https://doi.org/10.1021/acsami.3c16033
ACS Appl. Mater. Interfaces 2024, 16, 4430−4438

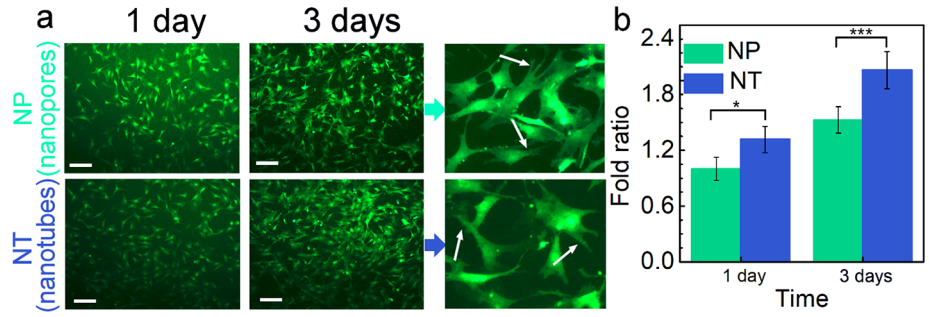

Figure 4. (a) Fluorescence images of GFP-labeled mesenchymal stem cells after 1 day of adhesion and 3 days of proliferation (scale bar 100 μm) at higher magnification to observe cell spreading and filopodia (arrows). (b) Cell adhesion at 1 day and proliferation at 3 days in culture on NP and NT. *: $p < 0.05$, ***: $p < 0.001$.

(2 or 4 M) leads to an NP structure, while at 5 M some separation into NTs at the top can already be identified, and at 6 M a NT structure is obtained. Of note is that the water content also influences the diameter of the nanostructure in a directly proportional manner (e.g., for 6 M, a ≈24 nm NT diameter); therefore, depending on the desired morphology, an equilibrium between the water content and anodization voltage is needed.

The current profiles of the selected NP and NT are shown in Figure 2b. Typically, for anodic NTs, the $I-t$ curve is divided into three regions: (i) a decrease in current due to oxide film coverage of the surface, (ii) a rise in current due to porosification (higher surface area), and (iii) a steady-state condition, where the oxide is continuously formed at the metal/oxide interface. These three regions are observed for the nanostructures of the present study, even at a low potential of 10 V (inset in Figure 2b).

For anodic nanostructured layers, the applied voltage is directly linked to the type of nanostructure (Figure 2c,d), including NPs, NTs, sponge formation, and electropolishing.[64] NPs can be grown at low voltages (5−10 V) in low water content electrolytes (2−8 M) containing ethylene glycol, while the anodization time can be varied between 45 min to 5 h (the increased water content or anodization voltage has to be compensated by decreasing the anodization time). The water content in the electrolyte and the applied voltage directly influenced the pore-wall-splitting transition (as shown for water content in Figure 2a). Although the influence of the applied voltage on the diameter is well established in literature,[2] here, we also point out a few selected conditions for NTs with diameters of 50, 80, and 100 nm (Figure 2d). Note that nanograss can be formed at higher voltages (and longer anodization times) owing to the chemical etching occurring at the NT top (Figure 2d, 100 V, 1.5 h, arrow). However, postultrasonication treatments under mild conditions lead to open-top nanotubes (Figure 2d, 120 V, 50 min with postultrasonication).

The as-formed NP and NT layers are amorphous (see the XRD patterns in Figure S3, showing only peaks corresponding to the metallic Ti substrate). The accumulation of fluorides at the cell boundaries and in a fluoride-rich layer and their selective chemical dissolution in aqueous electrolytes[65] is shown schematically in Figure 3a. The F content in the nanostructures is listed in Figure 2b, briefly, from EDX data (Figure S4a) a higher F content is observed in the NPs, due to the undissolved fluorine-rich layer (8.8. % compared to 3.1 atom % for NT), while XPS data confirms metal fluorides (≈685 eV[66]) in similar amount on the surface but in a significantly higher amount in the NPs' depth (Figure S4b,c). ToF-SIMS sputter depth profiles in negative polarity (Figures 3c and S5) show significant differences in the TiF_3^- and TiF_2^- mass fragments intensities (for more details, see Supporting Information and Figures S5 and S6). The morphological differences are also visible after partly sputtering through the nanostructures (SEM images in Figure 3c).

Surface wettability is one of the key parameters influencing biological responses to microenvironments surrounding the implanted biomaterials.[7] The TiO_2 nanostructures are hydrophilic and display a water contact angle (WCA) of 28° ± 1° (NP) and 36° ± 1° (NT) (Figure 3e), compared to the higher WCA value of 74° for Ti.[67] The WCA values for both nanostructures are aligned with literature data on the as-formed nanotubes, corresponding to their hydrophilic nature with contact angles between 20° and 40°.[67−69] Note that after aging the sample for one year (i.e., a simple storage of the samples), the WCA of the layers significantly increase toward hydrophobic values (Figure 3e), most likely due to carbon uptake from the environment. However, the hydrophilic characteristics of the TiO_2 nanostructures are restored after the removal of the contamination by briefly cleaning the samples (for example, by immersion in ethanol solution).

To investigate cell performance in response to these small-diameter NP and NT structures, human mesenchymal stem cells are seeded onto the surface of analyzed samples at a cell density of 5000 cm^{-2} (see Experimental Section for more details). After 24 h of incubation, cell adhesion is found to be slightly higher for NTs compared to that of NPs (Figure 4a). After 3 days of incubation on the TiO_2 nanostructures, enhanced cell proliferation is observed in the NT layers (Figure 4b). A typical spreading pattern of adherent mesenchymal cells, forming lamellopodia and filopodia, are observed on both NP and NT structures after 3 days of proliferation (see also the higher magnification in Figure 4a).

Our previous works[1,47] and additional literature[50] for NTs samples with UV sterilization or immersion in ethanol solution show a greater extent of focal contact formation on nanotubes with diameters smaller than 30 nm by the activation of integrin-mediated signaling pathways, resulting in the clustering of integrins and their optimal activation. In the current study, we further attempt to verify whether the lateral spacing structure surrounding the NTs, as opposed to the NPs, can affect the efficiency of stem cell anchorage on nanostructured substrates. For further insight for the higher cell adhesion and growth on the NT structure compared to NP (Figure 4), we specifically investigate integrin activation to compare cell anchorage between NPs and NTs. Using immunogold labeling

https://doi.org/10.1021/acsami.3c16033
ACS Appl. Mater. Interfaces 2024, 16, 4430−4438

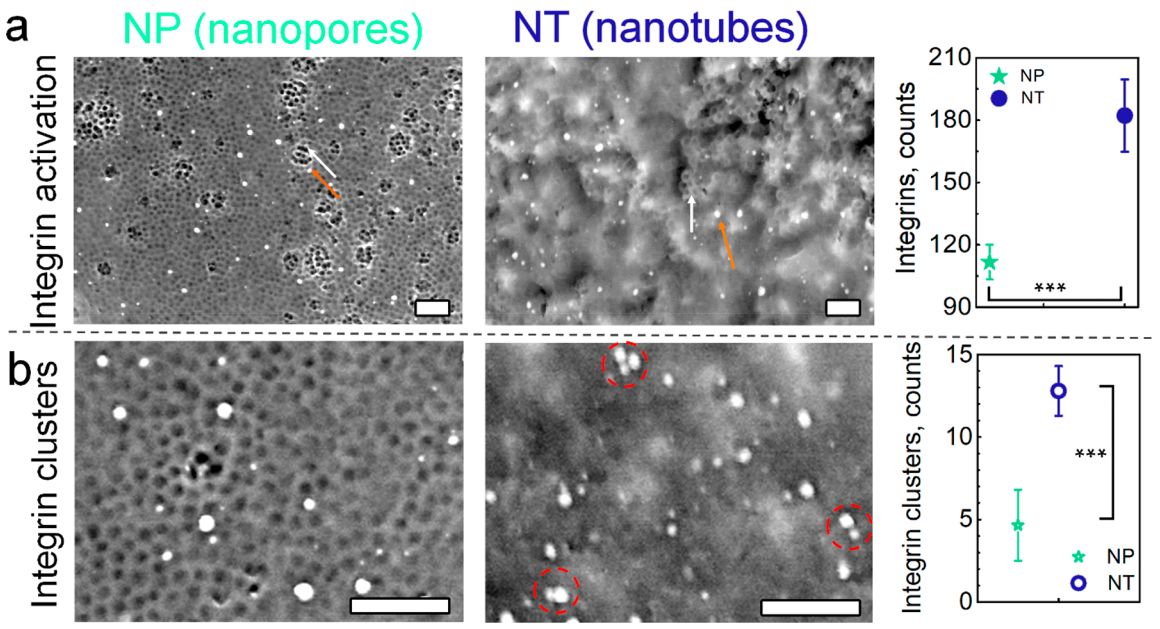

Figure 5. (a) Integrin activation on cell surface membrane (white arrow, NP or NT structure; orange arrow, cell membrane) and (b) integrin clustering on the NP and NT structures, determined by immunogold labeling with antibodies against β1 integrin under SEM observation (the integrin counts and activation were determined from 10 representative SEM images, 100k magnification, for each structure). Scale bars, 100 nm. ***: $p < 0.001$

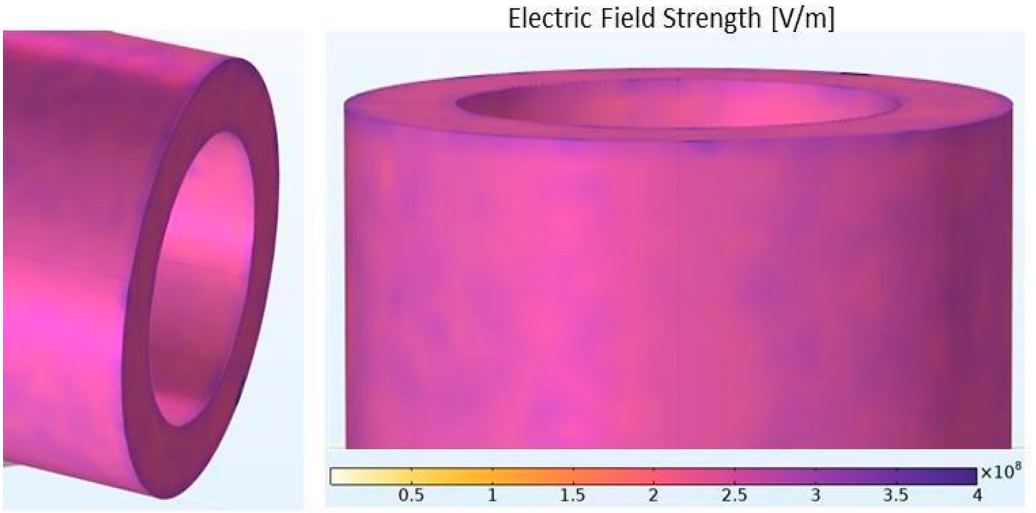

Figure 6. Calculated electric field distribution on the TiO_2 NTs surface in contact with the electrolyte solution. The model parameters were a bulk electrolyte concentration of 150 mmol/L and an electric potential of 110 mV.

with antibodies against β1 integrin, the integrins on the cell surface membrane and their clustering are observed under SEM (Figure 5a). Immunogold SEM images of cells on NPs and NTs clearly show that the cell membrane on the NT structure contains more integrins than for NPs. This observation is quantified in integrin activation, where on NTs, a count of 182 ± 17 integrins is obtained, compared to 111 ± 8.4 for NPs, thus resulting in 63% enhanced activation of integrin on the NTs. Moreover, the increased detection of integrin on NTs is accompanied by a typical, abundant integrin clustering (Figure 5b, dotted circles), with more than two integrins found in close proximity. Integrin clustering is more pronounced for NTs with a mean value of 12.8 ± 1.5 integrin clusters, as compared to 4.5 ± 2 clusters for NPs.

The above data show a significant difference in integrin clustering, with the NTs exhibiting an almost 3-fold higher number of clusters than the NP. In fact, it is not surprising that the results reveal a slight difference in cell adhesion between NPs and NTs (Figure 4). As discussed in the Introduction, previous studies have shown a higher stem cell adhesion on NTs with a diameter of less than 30 nm. Since a diameter smaller than 30 nm seems to be optimal for stem cell adhesion via integrin packaging, it is presumable that the initial cell adhesion would not be dramatically different on NP and NT structures, as both nanostructures in the present study have similar inner diameters. Surprisingly, the significant differences in integrin clustering shown in Figure 5 raise the possibility that the existing spacing between NTs (Figure 1d) might considerably affect differences in cell proliferation, integrin

https://doi.org/10.1021/acsami.3c16033
ACS Appl. Mater. Interfaces 2024, 16, 4430−4438

activation, and integrin clustering. In other words, the NT structure results in 37% more cell proliferation, 63% more integrin activation, and 163% more integrin clustering. We speculate that the spacing between NTs allows more integrin packing and clustering, leading to favorable cell anchoring and adhesion and a cell proliferation signal to the nucleus via a downstream integrin signaling pathway.

The literature shows that small-diameter NT structures with sharp edges of walls ensure increased electrostatic attraction of positively charged particles, increased electrostatic attraction of positive domains of particles with distinctive internal charge distribution, and stronger mediated interactions between charged-like TiO_2 and cell surfaces.[54,55] This results from the surface charge density occurring at the wall edge on the highly curved rims of the NT tops, which can, in turn, promote binding to a higher amount of positively charged proteins or proteins with an internal positive charge distribution.[3] Figure 6 shows a tube top with its curved rims and the corresponding calculated electric field strength, which is more pronounced at the sharp edge of the wall rim (see the magnitude at the edges). For the NP structure, half of the sharp edges of the wall rim were present (only the inner wall, compared to the NT structure with both inner and outer rim walls).

Subsequently, the surface charge densities at the inner edge wall, middle of the wall edge, and outer wall edge are evaluated. The results in Figure 7 correlate the surface charge

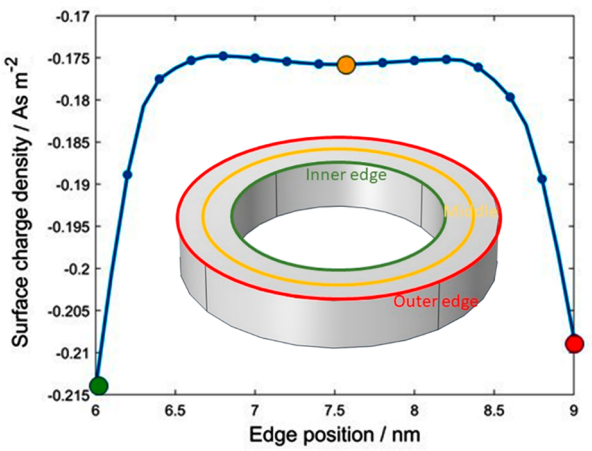

Figure 7. A schematic of the position of the inner edge, middle, and outer edge on the top NTs surface and the corresponding surface charge density as a function of the position on the wall rim (the inner edge, middle, and outer edge are denoted by dots in green, yellow, and red, respectively). The values of the model parameters are the same as those shown in Figure 6.

density (As m^{-2}) with the edge position (see the 3D schematic, inset image, and surface charge density). The data presented above clearly show that the magnitudes of the electric field (E) and surface charge density increase at the inner and outer sharp edges of the top surface of the NTs. In contrast, the NPs will only show approximately half of these values because they have twice as few sharp edges as the NTs.

4. CONCLUSIONS

Herein, we demonstrate and discuss the differences between anodic TiO_2 NPs and NTs in terms of their synthesis, physicochemical characterization, electrostatic properties, and cell interactions. NP and NT layers with similar diameters (15 nm) and tube lengths (500 nm) were obtained via electrochemical anodization in an organic-based electrolyte containing HF. At low anodization voltages (10 V), NP layers are initially formed, but as the anodization time increases, the NPs transition to NTs owing to a pore-wall splitting mechanism caused by the dissolution of the fluoride-rich layer. The fluoride content in the NPs is much higher than that of NTs throughout the layer, further confirming the presence of a fluoride-rich layer in the case of NPs. The NT layers showed slightly higher cell adhesion and proliferation; however, more significantly a 2-fold increase in integrin activation and a 3-fold increase in their clustering are observed. Additional electrostatic modeling shows that NTs have an increased electric field and surface charge density compared to those of NPs, and this aspect can further enhance cell interactions. These findings underscore the crucial significance of distinguishing between the NP and NT structures, shedding light on the factors influencing stem cell behavior and holding substantial implications for advancing biomedical substrate design and regenerative medicine.

■ ASSOCIATED CONTENT

Supporting Information

The Supporting Information is available free of charge at https://pubs.acs.org/doi/10.1021/acsami.3c16033.

Long-range order of nanostructures, XRD, EDX, and XPS results, and ToF-SIMS data (PDF)

■ AUTHOR INFORMATION

Corresponding Author

Anca Mazare − *Department of Materials Science WW4-LKO, Friedrich-Alexander University of Erlangen Nürnberg, 91054 Erlangen, Germany;* orcid.org/0000-0002-4836-946X; Email: anca.mazare@fau.de

Authors

Jung Park − *Division of Molecular Pediatrics, Department of Pediatrics, University Hospital Erlangen, 91054 Erlangen, Germany*

Alexander B. Tesler − *Department of Materials Science WW4-LKO, Friedrich-Alexander University of Erlangen Nürnberg, 91054 Erlangen, Germany;* orcid.org/0000-0003-3425-7667

Ekaterina Gongadze − *Laboratory of Physics, Faculty of Electrical Engineering, University of Ljubljana, Ljubljana SI-1000, Slovenia*

Aleš Iglič − *Laboratory of Physics, Faculty of Electrical Engineering, University of Ljubljana, Ljubljana SI-1000, Slovenia; Laboratory of Clinical Biophysics, Faculty of Medicine, University of Ljubljana, Ljubljana 1000, Slovenia*

Patrik Schmuki − *Department of Materials Science WW4-LKO, Friedrich-Alexander University of Erlangen Nürnberg, 91054 Erlangen, Germany; Regional Centre of Advanced Technologies and Materials, Czech Advanced Technology and Research Institute, Palacky University, Olomouc 779 00, Czech Republic;* orcid.org/0000-0002-9208-5771

Complete contact information is available at: https://pubs.acs.org/10.1021/acsami.3c16033

Author Contributions

#J.P. and A.M. contributed equally to this work.

https://doi.org/10.1021/acsami.3c16033
ACS Appl. Mater. Interfaces 2024, 16, 4430−4438

Notes

The authors declare no competing financial interest.

■ ACKNOWLEDGMENTS

J.P. and P.S. acknowledge the DFG (Grants 257236827, SCHM 1597/32-3, and PA 2537/13-1). A.B.T. acknowledges the DFG (Grant 442826449) for the financial support.

■ REFERENCES

(1) Park, J.; Bauer, S.; Von Der Mark, K.; Schmuki, P. Nanosize and Vitality: TiO2 Nanotube Diameter Directs Cell Fate. *Nano Lett.* **2007**, *7* (6), 1686−1691.
(2) Lee, K.; Mazare, A.; Schmuki, P. One-Dimensional Titanium Dioxide Nanomaterials: Nanotubes. *Chem. Rev.* **2014**, *114* (19), 9385−9454.
(3) Kulkarni, M.; Mazare, A.; Park, J.; Gongadze, E.; Killian, M. S.; Kralj, S.; von der Mark, K.; Iglič, A.; Schmuki, P. Protein Interactions with Layers of TiO2 Nanotube and Nanopore Arrays: Morphology and Surface Charge Influence. *Acta Biomater.* **2016**, *45*, 357.
(4) Geetha, M.; Singh, A. K.; Asokamani, R.; Gogia, A. K. Ti Based Biomaterials, the Ultimate Choice for Orthopaedic Implants - A Review. *Prog. Mater. Sci.* **2009**, *54* (3), 397−425.
(5) Zhang, L. C.; Chen, L. Y. A Review on Biomedical Titanium Alloys: Recent Progress and Prospect. *Adv. Eng. Mater.* **2019**, *21* (4), 1−29.
(6) Boyan, B. D.; Lotz, E. M.; Schwartz, Z. Roughness and Hydrophilicity as Osteogenic Biomimetic Surface Properties. *Tissue Eng. - Part A* **2017**, *23* (23−24), 1479−1489.
(7) Bauer, S.; Schmuki, P.; von der Mark, K.; Park, J. Engineering Biocompatible Implant Surfaces. Part I: Materials and Surfaces. *Prog. Mater. Sci.* **2013**, *58* (3), 261−326.
(8) Chamberlain, L. M.; Brammer, K. S.; Johnston, G. W.; Chien, S.; Jin, S. Macrophage Inflammatory Response to TiO2 Nanotube Surfaces. *J. Biomater. Nanobiotechnol.* **2011**, *02* (03), 293−300.
(9) Mas-Moruno, C.; Espanol, M.; Montufar, E. B.; Mestres, G.; Aparicio, C.; Gil, F. J.; Ginebra, M. P. Bioactive Ceramic and Metallic Surfaces for Bone Engineering. *Biomaterials Surface Science* **2013**, 337−374.
(10) Kurup, A.; Dhatrak, P.; Khasnis, N. Surface Modification Techniques of Titanium and Titanium Alloys for Biomedical Dental Applications: A Review. *Mater. Today Proc.* **2021**, *39* (xxxx), 84−90.
(11) Ion, R.; Necula, M. G.; Mazare, A.; Mitran, V.; Neacsu, P.; Schmuki, P.; Cimpean, A. Drug Delivery Systems Based on Titania Nanotubes and Active Agents for Enhanced Osseointegration of Bone Implants. *Curr. Med. Chem.* **2020**, *27* (6), 854−902.
(12) Neacsu, P.; Mazare, A.; Schmuki, P.; Cimpean, A. Attenuation of the Macrophage Inflammatory Activity by TiO2 Nanotubes via Inhibition of MAPK and NF-KB Pathways. *Int. J. Nanomedicine* **2015**, *10*, 6455−6467.
(13) Salamanna, F.; Gambardella, A.; Contartese, D.; Visani, A.; Fini, M. Nano-Based Biomaterials as Drug Delivery Systems against Osteoporosis: A Systematic Review of Preclinical and Clinical Evidence. *Nanomaterials* **2021**, *11* (2), 530.
(14) Xue, T.; Attarilar, S.; Liu, S.; Liu, J.; Song, X.; Li, L.; Zhao, B.; Tang, Y. Surface Modification Techniques of Titanium and Its Alloys to Functionally Optimize Their Biomedical Properties: Thematic Review. *Front. Bioeng. Biotechnol.* **2020**, *8*, 603072.
(15) Souza, J. C. M.; Sordi, M. B.; Kanazawa, M.; Ravindran, S.; Henriques, B.; Silva, F. S.; Aparicio, C.; Cooper, L. F. Nano-Scale Modification of Titanium Implant Surfaces to Enhance Osseointegration. *Acta Biomater.* **2019**, *94*, 112−131.
(16) Rodriguez-Contreras, A.; Guadarrama Bello, D.; Nanci, A. Surface Nanoporosity Has a Greater Influence on Osteogenic and Bacterial Cell Adhesion than Crystallinity and Wettability. *Appl. Surf. Sci.* **2018**, *445*, 255−261.
(17) Nazarov, D. V.; Smirnov, V. M.; Zemtsova, E. G.; Yudintceva, N. M.; Shevtsov, M. A.; Valiev, R. Z. Enhanced Osseointegrative Properties of Ultra-Fine-Grained Titanium Implants Modified by Chemical Etching and Atomic Layer Deposition. *ACS Biomater. Sci. Eng.* **2018**, *4* (9), 3268−3281.
(18) LIU, X.; CHU, P.; DING, C. Surface Modification of Titanium, Titanium Alloys, and Related Materials for Biomedical Applications. *Mater. Sci. Eng. R Reports* **2004**, *47* (3−4), 49−121.
(19) Hossain, M. F.; Naka, S.; Okada, H. Annealing Effect of E-Beam Evaporated TiO2 Films and Their Performance in Perovskite Solar Cells. *J. Photochem. Photobiol. A Chem.* **2018**, *360*, 109−116.
(20) Pantaroto, H. N.; Cordeiro, J. M.; Pereira, L. T.; de Almeida, A. B.; Nociti Junior, F. H.; Rangel, E. C.; Azevedo Neto, N. F.; da Silva, J. H. D.; Barão, V. A. R. Sputtered Crystalline TiO2 Film Drives Improved Surface Properties of Titanium-Based Biomedical Implants. *Mater. Sci. Eng., C* **2021**, *119*, No. 111638.
(21) Aghaee, M.; Verheyen, J.; Stevens, A. A. E.; Kessels, W. M. M.; Creatore, M. TiO2 Thin Film Patterns Prepared by Chemical Vapor Deposition and Atomic Layer Deposition Using an Atmospheric Pressure Microplasma Printer. *Plasma Process. Polym.* **2019**, *16* (12), 1900127.
(22) Liu, L.; Bhatia, R.; Webster, T. Atomic Layer Deposition of Nano-TiO2 Thin Films with Enhanced Biocompatibility and Antimicrobial Activity for Orthopedic Implants. *Int. J. Nanomedicine* **2017**, *12*, 8711−8723.
(23) Park, J.; Cimpean, A.; Tesler, A. B.; Mazare, A. Anodic TiO2 Nanotubes: Tailoring Osteoinduction via Drug Delivery. *Nanomaterials* **2021**, *11* (9), 2359.
(24) Guo, T.; Oztug, N. A. K.; Han, P.; Ivanovski, S.; Gulati, K. Untwining the Topography-Chemistry Interdependence to Optimize the Bioactivity of Nano-Engineered Titanium Implants. *Appl. Surf. Sci.* **2021**, *570*, No. 151083.
(25) Ozkan, S.; Nguyen, N. T.; Mazare, A.; Cerri, I.; Schmuki, P. Controlled Spacing of Self-Organized Anodic TiO2 Nanotubes. *Electrochem. commun.* **2016**, *69*, 76−79.
(26) Kafshgari, M. H.; Mazare, A.; Distaso, M.; Goldmann, W. H.; Peukert, W.; Fabry, B.; Schmuki, P. Intracellular Drug Delivery with Anodic Titanium Dioxide Nanotubes and Nanocylinders. *ACS Appl. Mater. Interfaces* **2019**, *11* (16), 14980−14985.
(27) Wei, W.; Berger, S.; Hauser, C.; Meyer, K.; Yang, M.; Schmuki, P. Transition of TiO2 Nanotubes to Nanopores for Electrolytes with Very Low Water Contents. *Electrochem. commun.* **2010**, *12* (9), 1184−1186.
(28) Liu, N.; Lee, K.; Schmuki, P. Small Diameter TiO2 Nanotubes vs. Nanopores in Dye Sensitized Solar Cells. *Electrochem. commun.* **2012**, *15* (1), 1−4.
(29) Yang, S.; Aoki, Y.; Habazaki, H. Effect of Electrolyte Temperature on the Formation of Self-Organized Anodic Niobium Oxide Microcones in Hot Phosphate−Glycerol Electrolyte. *Appl. Surf. Sci.* **2011**, *257* (19), 8190−8195.
(30) Lee, K.; Kim, D.; Schmuki, P. Highly Self-Ordered Nanochannel TiO2 Structures by Anodization in a Hot Glycerol Electrolyte. *Chem. Commun. (Camb).* **2011**, *47* (20), 5789−5791.
(31) Silverwood, R. K.; Fairhurst, P. G.; Sjöström, T.; Welsh, F.; Sun, Y.; Li, G.; Yu, B.; Young, P. S.; Su, B.; Meek, R. M. D.; Dalby, M. J.; Tsimbouri, P. M. Analysis of Osteoclastogenesis/Osteoblastogenesis on Nanotopographical Titania Surfaces. *Adv. Healthc. Mater.* **2016**, *5* (8), 947−955.
(32) Losic, D. Advancing of Titanium Medical Implants by Surface Engineering: Recent Progress and Challenges. *Expert Opin. Drug Delivery* **2021**, *18*, 1355.
(33) Wang, X.; Li, B.; Zhou, L.; Ma, J.; Zhang, X.; Li, H.; Liang, C.; Liu, S.; Wang, H. Influence of Surface Structures on Biocompatibility of TiO2/HA Coatings Prepared by MAO. *Mater. Chem. Phys.* **2018**, *215*, 339−345.
(34) Zhang, X.; Lv, Y.; Fu, S.; Wu, Y.; Lu, X.; Yang, L.; Liu, H.; Dong, Z. Synthesis, Microstructure, Anti-Corrosion Property and Biological Performances of Mn-Incorporated Ca-P/TiO2 Composite Coating Fabricated via Micro-Arc Oxidation. *Mater. Sci. Eng., C* **2020**, *117* (April), No. 111321.
(35) Du, Q.; Wei, D.; Cheng, S.; Wang, Y.; Li, B.; Jia, D.; Zhou, Y. Rapid Structural Evolution and Bone Inducing Mechanism of the

https://doi.org/10.1021/acsami.3c16033
ACS Appl. Mater. Interfaces 2024, 16, 4430−4438

Multilayer Coating with Silicon-Doped Hydroxyapatite Crystals on the Microwave Water Steaming-Hydrothermally Treated Titania Coating. *Appl. Surf. Sci.* **2021**, *539*, No. 148153.
(36) Motola, M.; Capek, J.; Zazpe, R.; Bacova, J.; Hromadko, L.; Bruckova, L.; Ng, S.; Handl, J.; Spotz, Z.; Knotek, P.; Baishya, K.; Majtnerova, P.; Prikryl, J.; Sopha, H.; Rousar, T.; Macak, J. M. Thin TiO 2 Coatings by ALD Enhance the Cell Growth on TiO 2 Nanotubular and Flat Substrates. *ACS Appl. Bio Mater.* **2020**, *3* (9), 6447−6456.
(37) Farsinezhad, S.; Waghmare, P. R.; Wiltshire, B. D.; Sharma, H.; Amiri, S.; Mitra, S. K.; Shankar, K. Amphiphobic Surfaces from Functionalized TiO2 Nanotube Arrays. *RSC Adv.* **2014**, *4* (63), 33587−33598.
(38) Pan, C.; Liu, T.; Yang, Y.; Liu, T.; Gong, Z.; Wei, Y.; Quan, L.; Yang, Z.; Liu, S. Incorporation of Sr2+ and Ag Nanoparticles into TiO2 Nanotubes to Synergistically Enhance Osteogenic and Antibacterial Activities for Bone Repair. *Mater. Des.* **2020**, *196*, No. 109086.
(39) Bauer, S.; Park, J.; Pittrof, A.; Song, Y.-Y.; von der Mark, K.; Schmuki, P. Covalent Functionalization of TiO2 Nanotube Arrays with EGF and BMP-2 for Modified Behavior towards Mesenchymal Stem Cells. *Integr. Biol. (Camb).* **2011**, *3* (9), 927−936.
(40) Sopha, H.; Bacova, J.; Baishya, K.; Sepúlveda, M.; Rodriguez-Pereira, J.; Capek, J.; Hromadko, L.; Zazpe, R.; Thalluri, S. M.; Mistrik, J.; Knotek, P.; Rousar, T.; Macak, J. M. White and Black Anodic TiO2 Nanotubes: Comparison of Biological Effects in A549 and SH-SY5Y Cells. *Surf. Coat. Technol.* **2023**, *462*, No. 129504.
(41) Mazare, A.; Park, J.; Simons, S.; Mohajernia, S.; Hwang, I.; Yoo, J. E.; Schneider, H.; Fischer, M. J.; Schmuki, P. Black TiO2 Nanotubes: Efficient Electrodes for Triggering Electric Field-Induced Stimulation of Stem Cell Growth. *Acta Biomater.* **2019**, *97*, 681−688.
(42) Baishya, K.; Vrchovecká, K.; Alijani, M.; Rodriguez-Pereira, J.; Thalluri, S. M.; Goldbergová, M. P.; Přibyl, J.; Macak, J. M. Bio-AFM Exploits Enhanced Response of Human Gingival Fibroblasts on TiO2 Nanotubular Substrates with Thin TiO2 Coatings. *Appl. Surf. Sci. Adv.* **2023**, *18*, No. 100459.
(43) Shen, Z.; Wang, S.; Shen, Z.; Tang, Y.; Xu, J.; Lin, C.; Chen, X.; Huang, Q. Deciphering Controversial Results of Cell Proliferation on TiO2 Nanotubes Using Machine Learning. *Regen. Biomater.* **2021**, *8* (4), rbab025.
(44) Junkar, I.; Kulkarni, M.; Drašler, B.; Rugelj, N.; Mazare, A.; Flašker, A.; Drobne, D.; Humpolíček, P.; Resnik, M.; Schmuki, P.; Mozetič, M.; Iglič, A. Influence of Various Sterilization Procedures on TiO2 Nanotubes Used for Biomedical Devices. *Bioelectrochemistry* **2016**, *109*, 79−86.
(45) Guo, T.; Oztug, N. A. K.; Han, P.; Ivanovski, S.; Gulati, K. Influence of Sterilization on the Performance of Anodized Nanoporous Titanium Implants. *Mater. Sci. Eng., C* **2021**, *130*, No. 112429.
(46) Park, J.; Bauer, S.; Schmuki, P.; Von Der Mark, K. Narrow Window in Nanoscale Dependent Activation of Endothelial Cell Growth and Differentiation on TiO2 Nanotube Surfaces. *Nano Lett.* **2009**, *9* (9), 3157−3164.
(47) Park, J.; Bauer, S.; Schlegel, K. A.; Neukam, F. W.; von der Mark, K.; Schmuki, P. TiO2 Nanotube Surfaces: 15 Nm - an Optimal Length Scale of Surface Topography for Cell Adhesion and Differentiation. *Small* **2009**, *5* (6), 666−671.
(48) Park, J.; Bauer, S.; Pittrof, A.; Killian, M. S.; Schmuki, P.; von der Mark, K. Synergistic Control of Mesenchymal Stem Cell Differentiation by Nanoscale Surface Geometry and Immobilized Growth Factors on TiO2 Nanotubes. *Small* **2012**, *8* (1), 98−107.
(49) Bauer, S.; Park, J.; Faltenbacher, J.; Berger, S.; von der Mark, K.; Schmuki, P. Size Selective Behavior of Mesenchymal Stem Cells on ZrO(2) and TiO(2) Nanotube Arrays. *Integr. Biol. (Camb).* **2009**, *1* (8−9), 525−532.
(50) Brammer, K. S.; Oh, S.; Cobb, C. J.; Bjursten, L. M.; van der Heyde, H.; Jin, S. Improved Bone-Forming Functionality on Diameter-Controlled TiO2 Nanotube Surface. *Acta Biomater.* **2009**, *5* (8), 3215−3223.
(51) Li, Y.; Wang, S.; Dong, Y.; Mu, P.; Yang, Y.; Liu, X.; Lin, C.; Huang, Q. Effect of Size and Crystalline Phase of TiO2 Nanotubes on Cell Behaviors: A High Throughput Study Using Gradient TiO2 Nanotubes. *Bioact. Mater.* **2020**, *5* (4), 1062−1070.
(52) Khaw, J. S.; Bowen, C. R.; Cartmell, S. H. Effect of TiO2 Nanotube Pore Diameter on Human Mesenchymal Stem Cells and Human Osteoblasts. *Nanomaterials* **2020**, *10* (11), 2117.
(53) Park, J.; Setter, V.; Wixler, V.; Schneider, H. Umbilical Cord Blood Stem Cells: Induction of Differentiation into Mesenchymal Lineages by Cell−Cell Contacts with Various Mesenchymal Cells. *Tissue Eng. Part A* **2009**, *15* (2), 397−406.
(54) Iglic, A.; Gongadze; Kabaso, D.; Bauer; Schmuki, P.; Slivnik; van Rienen, U. Adhesion of Osteoblasts to a Nanorough Titanium Implant Surface. *Int. J. Nanomedicine* **2011**, *6*, 1801.
(55) Gongadze, E.; Velikonja, A.; Perutkova, Š.; Kramar, P.; Maček-Lebar, A.; Kralj-Iglič, V.; Iglič, A. Ions and Water Molecules in an Electrolyte Solution in Contact with Charged and Dipolar Surfaces. *Electrochim. Acta* **2014**, *126*, 42−60.
(56) Ali, G.; Chen, C.; Yoo, S. H.; Kum, J. M.; Cho, S. O. Fabrication of Complete Titania Nanoporous Structures via Electrochemical Anodization of Ti. *Nanoscale Res. Lett.* **2011**, *6* (1), 1−10.
(57) Mazare, A. Comment on "Old Is Gold: Electrolyte Aging Influences the Topography, Chemistry, and Bioactivity of Anodized TiO2Nanopores.". *ACS Appl. Mater. Interfaces* **2022**, *14* (13), 14837−14841.
(58) Wang, F.; Liu, Y.; Dong, W.; Shen, M.; Kang, Z. Tuning TiO2 Photoelectrochemical Properties by Nanoring/Nanotube Combined Structure. *J. Phys. Chem. C* **2011**, *115* (30), 14635−14640.
(59) Zhang, Z.; Yu, Y.; Wang, P. Hierarchical Top-Porous/Bottom-Tubular TiO2 Nanostructures Decorated with Pd Nanoparticles for Efficient Photoelectrocatalytic Decomposition of Synergistic Pollutants. *ACS Appl. Mater. Interfaces* **2012**, *4* (2), 990−996.
(60) Shin, Y.; Lee, S. Self-Organized Regular Arrays of Anodic TiO2 Nanotubes. *Nano Lett.* **2008**, *8* (10), 3171−3173.
(61) Jarosz, M.; Pawlik, A.; Szuwarzyński, M.; Jaskuła, M.; Sulka, G. D. Nanoporous Anodic Titanium Dioxide Layers as Potential Drug Delivery Systems: Drug Release Kinetics and Mechanism. *Colloids Surfaces B Biointerfaces* **2016**, *143*, 447−454.
(62) Guo, T.; Oztug, N. A. K.; Han, P.; Ivanovski, S.; Gulati, K. Old Is Gold: Electrolyte Aging Influences the Topography, Chemistry, and Bioactivity of Anodized TiO2 Nanopores. *ACS Appl. Mater. Interfaces* **2021**, *13* (7), 7897−7912.
(63) Sopha, H.; Hromadko, L.; Nechvilova, K.; Macak, J. M. Effect of Electrolyte Age and Potential Changes on the Morphology of TiO2 Nanotubes. *J. Electroanal. Chem.* **2015**, *759*, 122−128.
(64) Albu, S. P.; Roy, P.; Virtanen, S.; Schmuki, P. Self-Organized TiO2 Nanotube Arrays: Critical Effects on Morphology and Growth. *Isr. J. Chem.* **2010**, *50* (4), 453−467.
(65) Roy, P.; Berger, S.; Schmuki, P. TiO2 Nanotubes: Synthesis and Applications. *Angew. Chemie - Int. Ed.* **2011**, *50* (13), 2904−2939.
(66) Wanger, C. D.; Riggs, W. M.; Davis, L. E.; Moulder, J. F.; Muilenberg, G. E. *Handbook of X-Ray Photoelectron Spectroscopy*; Perkin-Elmer Corp.: Eden Prairie, MN, USA, 1992.
(67) Mazare, A.; Totea, G.; Burnei, C.; Schmuki, P.; Demetrescu, I.; Ionita, D. Corrosion, Antibacterial Activity and Haemocompatibility of TiO2 Nanotubes as a Function of Their Annealing Temperature. *Corros. Sci.* **2016**, *103*, 215−222.
(68) Balaur, E.; Macak, J. M.; Tsuchiya, H.; Schmuki, P. Wetting Behaviour of Layers of TiO2 Nanotubes with Different Diameters. *J. Mater. Chem.* **2005**, *15* (42), 4488−4491.
(69) Liu, G.; Du, K.; Wang, K. Surface Wettability of TiO2 Nanotube Arrays Prepared by Electrochemical Anodization. *Appl. Surf. Sci.* **2016**, *388*, 313−320.

https://doi.org/10.1021/acsami.3c16033
ACS Appl. Mater. Interfaces 2024, 16, 4430−4438